DOI: 10.14814/phy2.14568

ORIGINAL RESEARCH

Physiological Reports

Electrophysiological characterization of the modified $hERG_T$ potassium channel used to obtain the first cryo-EM hERG structure

Yihong Zhang[1] | **Christopher E. Dempsey**[2] | **Jules C. Hancox**[1]

[1]School of Physiology and Pharmacology and Neuroscience, Biomedical Sciences Building, The University of Bristol, University Walk, Bristol, UK

[2]School of Biochemistry, Biomedical Sciences Building, The University of Bristol, University Walk, Bristol, UK

Correspondence
Jules C. Hancox, School of Physiology and Pharmacology and Neuroscience, Biomedical Sciences Building, The University of Bristol, University Walk, Bristol, BS8 1TD UK.
Email: jules.hancox@bristol.ac.uk

Funding information
British Heart Foundation, Grant/Award Number: PG/17/89/33414

Abstract

The voltage-gated hERG (*human-Ether-à-go-go Related Gene*) K^+ channel plays a fundamental role in cardiac action potential repolarization. Loss-of-function mutations or pharmacological inhibition of hERG leads to long QT syndrome, whilst gain-of-function mutations lead to short QT syndrome. A recent open channel cryo-EM structure of hERG represents a significant advance in the ability to interrogate hERG channel structure-function. In order to suppress protein aggregation, a truncated channel construct of hERG ($hERG_T$) was used to obtain this structure. In $hERG_T$ cytoplasmic domain residues 141 to 350 and 871 to 1,005 were removed from the full-length channel protein. There are limited data on the electrophysiological properties of $hERG_T$ channels. Therefore, this study was undertaken to determine how $hERG_T$ influences channel function at physiological temperature. Whole-cell measurements of hERG current (I_{hERG}) were made at 37°C from HEK 293 cells expressing wild-type (WT) or $hERG_T$ channels. With a standard +20 mV activating command protocol, neither end-pulse nor tail I_{hERG} density significantly differed between WT and $hERG_T$. However, the I_{hERG} deactivation rate was significantly slower for $hERG_T$. Half-maximal activation voltage ($V_{0.5}$) was positively shifted for $hERG_T$ by ~+8 mV ($p < .05$ versus WT), without significant change to the activation relation slope factor. Neither the voltage dependence of inactivation, nor time course of development of inactivation significantly differed between WT and $hERG_T$, but recovery of I_{hERG} from inactivation was accelerated for $hERG_T$ ($p < .05$ versus WT). Steady-state "window" current was positively shifted for $hERG_T$ with a modest increase in the window current peak. Under action potential (AP) voltage clamp, $hERG_T$ I_{hERG} showed modestly increased current throughout the AP plateau phase with a significant increase in current integral during the AP. The observed consequences for $hERG_T$ I_{hERG} of deletion of the two cytoplasmic regions may reflect changes to electrostatic interactions influencing the voltage sensor domain.

KEYWORDS
hERG, I_{Kr}, KCNH2, Kv11.1, Long QT Syndrome, LQT2, potassium channel, rapid delayed rectifier

1 | INTRODUCTION

Cardiac action potential repolarization involves the coordinated activity of several key potassium (K^+) ion channels (Tamargo, Caballero, Gomez, Valenzuela, & Delpon, 2004). The rapid delayed rectifier K^+ current, I_{Kr}, plays an important role in repolarization from ventricular action potential (AP) plateau voltages, with current progressively increasing during the plateau before declining during terminal repolarization (Hancox, Levi, & Witchel, 1998; Mitcheson & Hancox, 1999; Rocchetti, Besana, Gurrola, Possani, & Zaza, 2001; Sanguinetti & Tristani-Firouzi, 2006). This final repolarization phase is mediated by the distinct, inwardly rectifying K^+ current, I_{K1} (Mitcheson & Hancox, 1999; Shimoni, Clark, & Giles, 1992; Zaza, Rochetti, Brioschi, Cantadori, & Ferroni, 1998). In addition to contributing to repolarization during APs, I_{Kr} can regulate diastolic depolarization of cells in pacemaker regions of the cardiac conduction system, through continued deactivation of I_{Kr} following AP repolarization (Mitcheson & Hancox, 1999; Ono & Ito, 1995). I_{Kr} is carried by channels encoded by *human-Ether-à-go-go Related Gene* (*hERG*, alternative nomenclature *KCNH2*) (Sanguinetti, Jiang, Curran, & Keating, 1995; Trudeau, Warmke, Ganetzky, & Robertson, 1995). hERG channel current (I_{hERG}), like I_{Kr}, is characterized by rapid voltage-dependent inactivation, which plays a critical role in shaping the channel's contribution to ventricular AP repolarization (Hancox, McPate, El Harchi, & Zhang, 2008; Sanguinetti & Tristani-Firouzi, 2006; Vandenberg, Walker, & Campbell, 2001). The channel's relatively fast inactivation/recovery from inactivation kinetics together with slower deactivation kinetics also means that hERG/I_{Kr} channels can generate outward transient currents that oppose premature stimuli late in repolarization/early in diastole (Lu et al., 2001; Vandenberg et al., 2001).

Given the important physiological roles of hERG/I_{Kr} channels, it is unsurprising that *hERG* mutations have adverse consequences. Loss-of-function *hERG* mutations underpin the LQT2 form of congenital long QT syndrome (LQTS), whilst gain-of-function mutations underlie the SQT1 form of congenital short QT syndrome (SQTS); both conditions predispose to malignant arrhythmias and sudden death (Hancox, Whittaker, Du, Stuart, & Zhang, 2018; Sanguinetti & Tristani-Firouzi, 2006). hERG channels also have a remarkable sensitivity to pharmacological inhibition by diverse pharmaceuticals linked to the drug-induced form of acquired LQTS (Hancox et al., 2008; Sanguinetti & Tristani-Firouzi, 2006). Due to this, novel pharmaceuticals must be tested for activity against the hERG channel (Gintant, 2008; Hancox et al., 2008). Current understanding of hERG channel structure-function has derived from a combination of functional mutagenesis studies and in silico modeling. For most of the period since the first electrophysiological studies of hERG in 1995 (Sanguinetti et al., 1995; Trudeau et al., 1995), in silico reconstructions of hERG structure have relied on homology modeling; in 2017 this changed with the publication of the first cryo electron microscopy (cryo-EM)-derived hERG structure (Wang & MacKinnon, 2017). This structure, of an open channel with voltage sensors captured in a depolarized conformation, provides unprecedented opportunities to better understand hERG channel gating and pharmacology (Butler, Helliwell, Zhang, Hancox, & Dempsey, 2020; Robertson & Morais-Cabral, 2019). It is important to note, however, that because the full-length wild-type (WT) hERG protein tends to aggregate during purification (Su, Brown, Wang, & MacKinnon, 2016; Wang & MacKinnon, 2017), the wild-type hERG construct used to obtain the cryo-EM structure contained deletions of two segments of the channel (see Figure 1a; residues 141–350 and 871–1005), each predicted to be disordered (Wang & MacKinnon, 2017). I_{hERG} kinetics data for the truncated construct, $hERG_T$, are limited to date, showing a modest (+5 mV) shift in voltage-dependent activation, whilst the channel retained sensitivity to inhibition by the high affinity inhibitors dofetilide and astemizole (Wang & MacKinnon, 2017). A question arises, therefore, as to the extent to which the kinetics of I_{hERG} carried by $hERG_T$ resemble or differ from those of the intact WT channel. Consequently, this study was undertaken to compare I_{hERG} carried by intact hERG with that carried by $hERG_T$.

2 | METHODS

2.1 | Mutagenesis

The $hERG_T$ 814 amino acid truncation construct in which two segments of the complete 1,159 amino acid protein (141–350 and 871–1005) were deleted (Wang & MacKinnon, 2017), was generated by Mutagenex Inc (Suwanee, GA 30,024, USA) from a WT hERG construct template in a vector of modified pcDNA3 used in our laboratory. Competent DH5α *Escherichia coli* (Invitrogen, Paisley, UK) were transformed using standard procedures, DNA was purified using a Endotoxin-free plasmid DNA purification kit

(Neumann-Neander-Str., Germany, Macherey-Nagel), and the mutation was confirmed by sequencing of the entire open reading frame (Eurofins MWG Operon, Ebersberg, Germany).

2.2 | Cell culture and transfection

Human embryonic kidney (HEK 293) cells (European Collection of Cell Cultures, Porton Down, UK) were used to study the effects of the WT and $hERG_T$ on I_{hERG} kinetics and profile under action potential (AP) voltage clamp. These cells were maintained at 37°C, 5% CO_2 in Dulbecco's minimum essential medium with Glutamax-1 (DMEM; Gibco, Paisley, UK). This was supplemented with 10% fetal bovine serum. Cells were transiently transfected with 1μg of cDNA plasmids encoding WT or $hERG_T$ using Lipofectamine 2000 (Invitrogen, Paisley, UK) according to the manufacturer's instructions. Expression plasmid encoding CD8 (0.15μg) was also added (in pIRES, donated by Dr I Baró, University of Nantes, France) to be used as a successful marker of transfection. Successfully transfected cells (positive to CD8) were identified using Dynabeads® (Invitrogen, Paisley, UK). This approach, which utilizes polystyrene microspheres coated with CD8 antibody that adhere to $CD8^+$ cells, has long been proposed to be valuable for visual identification of transfected cells for electrophysiology experiments (Jurman, Boland, Liu, & Yellen, 1994). Electrophysiological recording experiments were performed 12–48 hr after transfection (a range within that of prior studies from our laboratory; Butler, Zhang, Stuart, Dempsey, & Hancox, 2019; Melgari et al., 2015; Zhang et al., 2016).

2.3 | Solutions for electrophysiological recordings

Once the coverslip containing cells was put in the recording chamber, cells were superfused with normal Tyrode's containing (in mM): 140 NaCl, 4 KCl, 2.5 $CaCl_2$, 1 $MgCl_2$, 10 Glucose, and 5 HEPES (titrated to pH of 7.45 with NaOH) (Butler et al., 2019; Melgari et al., 2015; Zhang et al., 2016). The pipette dialysis solution for hERG current (I_{hERG}) measurement contained (in mM): 130 KCl, 1 $MgCl_2$, 5 EGTA, 5 MgATP, and 10 HEPES (titrated to a pH of 7.2 with KOH) (Butler et al., 2019; Melgari et al., 2015; Zhang et al., 2016).

2.4 | Experimental protocols

Whole-cell conventional and human AP voltage clamp ("AP clamp") recordings of I_{hERG} were made at 37 ± 1°C by using an Axopatch 200B amplifier (Axon Instruments, Foster City, CA, USA). Patch pipettes were fire polished to 2.5–4 MΩ. Between 70% and 80% of the electrode series resistance could be compensated. Data were recorded via a Digidata 1440A interface (Molecular Devices, Sunnyvale, CA, USA). Data digitization rates were 10–25 kHz during all protocols and an appropriate bandwidth of 2–10kHz was set on the amplifier. Currents elicited under "AP clamp" were corrected online for P/N leak subtraction using an interspersed P/4 protocol (Butler, Zhang, Stuart, Dempsey, & Hancox, 2018; McPate et al., 2009; Melgari et al., 2015). The specific voltage protocols used experimentally are detailed within the relevant figures and associated Results.

Half-maximal activation ($V_{0.5}$) voltage values were obtained by normalizing I_{hERG} tail values (I) at −40 mV following differing voltage commands to the maximal I_{hERG} tail value observed during the voltage protocol (Imax). The resulting values were plotted against corresponding command voltage (Vm), and fitted by a Boltzmann equation of the form:

$$I/I_{max} = 1/\left(1+\exp\left(\left(V_{0.5}-Vm\right)/k\right)\right) \quad (1)$$

Half-maximal inactivation voltage ($V_{0.5}$) was obtained from normalized plots of voltage-dependent availability, using the following equation:

$$\text{Inactivation parameter} = 1-\left(1/\left(1+\exp\left[\left(V_{0.5}-Vm\right)/k\right]\right)\right) \quad (2)$$

Where the inactivation parameter occurs within the range 0 – 1, Vm represents the repolarization voltage used to influence I_{hERG} availability, $V_{0.5}$ is the half-maximal inactivation voltage and k is the slope factor describing the I_{hERG} inactivation relation.

Continuous plots of voltage-dependent activation and inactivation relations were obtained from half-maximal activation/inactivation voltage ($V_{0.5}$) and slope factor (k) values derived from experimental data, by calculation of activation and inactivation parameter values at 2 mV intervals between −150 and +100 mV, using equations 1 and 2 (Colenso, Sessions, Zhang, Hancox, & Dempsey, 2013; Zhang, Colenso, Sessions, Dempsey, & Hancox, 2011).

Action potential (AP) clamp experiments were conducted, as described previously, using a human epicardial ventricular AP waveform generated by the ten Tusscher–Noble–Noble–Panfilov ventricular tissue model (ten McPate et al., 2009; Tusscher, Noble, Noble, & Panfilov, 2004).

2.5 | Data presentation and statistical analysis

Data were analyzed using Clampfit 10.2 (Axon Instruments), Excel 2016 (Microsoft, Redmond, WA), Origin 2018b (OriginLab Corporation, Northampton, MA, USA), and Prism

8 (Graphpad Inc, La Jolla, CA, USA) software. Total charge carried by WT and $hERG_T$ channels during AP commands was determined by integrating currents using Origin 2018b (Butler et al., 2018). Statistical comparisons were made using the Student's *t* test, or two way analysis of variance (ANOVA) followed by Bonferroni *post hoc* test, as appropriate. *P* values less than 0.05 were taken as being statistically significant.

3 | RESULTS

3.1 | I_{hERG} carried by $hERG_T$ channels during a standard voltage "step" protocol

Figure 1a illustrates the truncated $hERG_T$ construct compared with WT hERG. The first deleted region encoding residues 141–350 (cut between 140 and 351), removed most of the N-linker region that connects the N terminal Per-ARNT-Sim (PAS) domain with S1 of the voltage sensor domain (VSD); the second deleted region encoding residues 871–1005 (cut between 870 to 1,006), eliminated much of the long cytoplasmic C terminal tail that follows the cytoplasmic cyclic nucleotide binding homology domain (CNBHD). In initial experiments, the profile of I_{hERG} was compared between WT and $hERG_T$ channels using a standard I_{hERG} protocol comprised of a 2 s depolarization from −80 to +20 mV, followed by repolarization to −40 mV. A brief (50 ms) prepulse from −80 to −40 mV preceded the +20 mV command, to provide a reference value for I_{hERG} tail amplitude measurement (Melgari et al., 2015; Zhang et al., 2016) WT I_{hERG} (Figure 1b, left panel) exhibited well-established characteristics: current development during the applied depolarization with a resurgent I_{hERG} "tail" elicited during a repolarizing step to −40 mV. I_{hERG} carried by $hERG_T$ (Figure 1b, right panel) exhibited a similar overall profile. The I_{hERG} tail and end-pulse current density were respectively 151.40 ± 22.28 pA/pF and 83.43 ± 13.93 pA/pF for $hERG_T$ ($n = 21$); for WT hERG the comparable values were 169.48 ± 25.10 pA/pF and 81.92 ± 12.65 pA/pF, respectively ($n = 21$). There was no significant difference in either value between WT and $hERG_T$ ($p = .59$ and 0.94 for tail and end-pulse current density respectively, Student's *t* test). Tail current deactivation was fitted with a biexponential function to derive fast and slow (τ_f and τs) time constant values (Zhou et al., 1998) (Figure 1c). The mean τ_s value (describing the slow component of deactivation) was significantly larger for I_{hERG} carried by $hERG_T$ than WT channels (1.73 ± 0.14 s for $hERG_T$ and 1.35 ± 0.09 s for WT, $p < .05$; $n = 21$ for each, Student's *t* test). τ_f and the relative proportion of fast/slow deactivation showed no significant change compared to WT ($p = .63$ and 0.59 respectively, Student's *t* test). Thus, $hERG_T$ slowed I_{hERG} deactivation by increasing τs.

3.2 | WT and $hERG_T$ current–voltage (I–V) relationships compared

The voltage dependence of WT and $hERG_T$ I_{hERG} was compared using 2 s depolarizing voltage steps from a holding

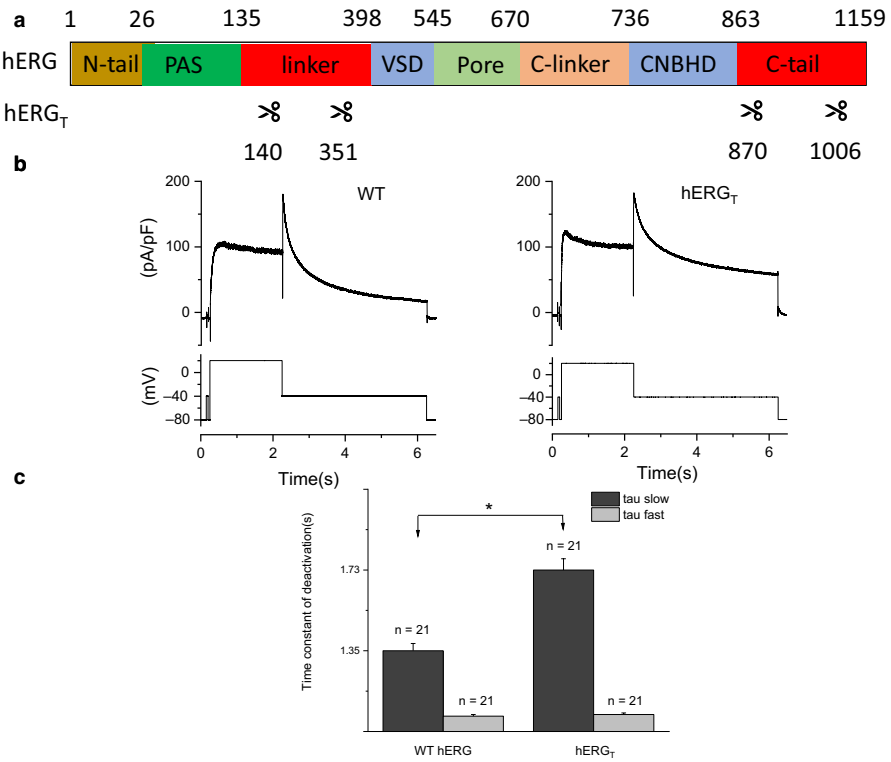

FIGURE 1 $hERG_T$ structure, current profile, and deactivation. (a) Schematic diagram showing truncated $hERG_T$ compared to WT hERG domains (indicated by use of different colors). In $hERG_T$, amino acid residues between 140–351 and 870–1006 were removed (regions encoding residues 141–350 and 871–1005 were removed). (b) Example current (I_{hERG}) traces for WT hERG (left panel) and $hERG_T$ (right panel) with corresponding voltage protocol shown in the lower panels. (c) Bar chart shows comparison of fast and slow deactivation time constants between WT and $hERG_T$ ($n = 21$ for each of WT and $hERG_T$, * denotes statistical significance of $p < .05$; unpaired *t* test)

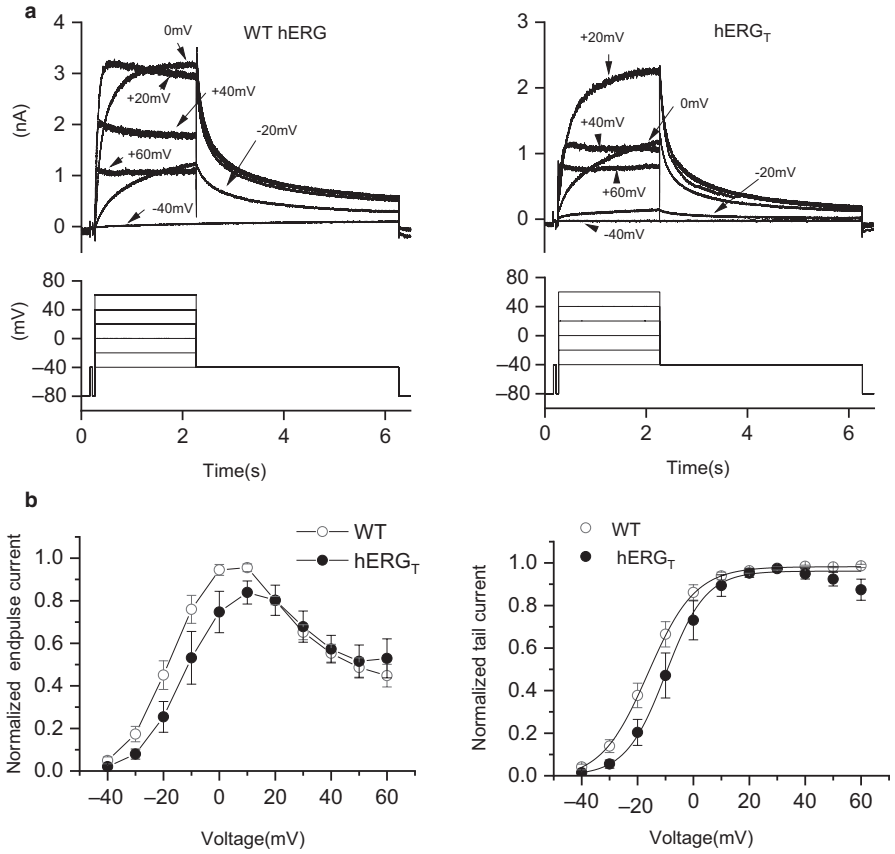

FIGURE 2 Current–voltage (I–V) relationship for WT and hERG$_T$ $I_{hERG.}$ (a) Upper panels show representative I_{hERG} families of currents for WT hERG (left panel) and hERG$_T$ (right panel). Test pulses were applied at 10 mV increments between −40 mV and +60 mV, with only selected traces being shown for clarity of display. Corresponding test potentials of the voltage protocol are indicated in the lower panel (start-to-start interval of 12 s between successive voltage steps). (b) Mean I–V relations for end-pulse currents (left panel) and mean normalized tail currents I–V relations (right panel); for each of WT ($n = 9$) and hERG$_T$ ($n = 7$), data were normalized to the maximal currents recorded during the protocol. Tail current data were fitted with equation 1 to give the $V_{0.5}$ and k values provided in the Results text.

potential of −80 mV to potentials between −40 and +60 mV (Butler et al., 2019; Zhang et al., 2011). Representative traces at selected potentials are shown in Figure 2a for WT (upper left panel) and hERG$_T$ (upper right panel) I_{hERG}, with the corresponding voltage protocol underneath. The normalized mean I–V data are shown in Figure 2b. For WT $I_{hERG,}$ the end-pulse current increased progressively with depolarization up to ~ 0mV, declining after 10 mV, giving rise to a well-established bell shaped current–voltage (I–V) relation (Figure 2b, left panel). For hERG$_T$, the I–V relation showed a similar profile, but peaked at +10 mV, with an apparent modest rightward shift of the end-pulse I–V relation compared to WT hERG. 2-way ANOVA analysis did not reveal overall significant differences between WT and hERG$_T$ in the normalized end-pulse I–V relations ($p = .11$). However, such analysis did show an overall significant difference between WT and hERG$_T$ in the normalized tail I–V relations ($p < .05$), although the conservative Bonferroni post-test did not identify significance at particular potentials in the tested range.

Scrutiny of the representative traces for WT and hERG$_T$ I_{hERG} in Figure 2a shows that for test voltages up to ~0 mV, hERG$_T$ I_{hERG} was activated to smaller extent than was that for WT hERG. Normalized I–V relations for I_{hERG} tails were used to quantify voltage-dependent activation, with fits to equation 1 used to derive half-maximal activation voltage ($V_{0.5}$) and slope (k) values (right panel of Figure 2b). The $V_{0.5}$ and k values for WT I_{hERG} activation derived from the fits were −15.96 ± 1.89mV and 7.52 ± 0.55mV ($n = 9$). For hERG$_T$ the comparable values were: −8.29 ± 3.10mV and 5.47 ± 1.01mV, respectively ($n = 7$; $p < .05$ for $V_{0.5}$ and $p = .11$ for k versus WT, Student's t test). Thus, the $V_{0.5}$ describing the voltage dependence of activation of I_{hERG} for hERG$_T$ was significantly shifted by ~+8mV compared to the WT channel (*cf* ~+5 mV reported by Wang & MacKinnon, 2017). This rightward shift in voltage-dependent activation of hERG$_T$ was associated with a slower rise-time of currents during the activating command at some voltages. Thus, exponential fitting of the current activated by the test pulse to −10 mV yielded rise-time τ values of 930.85 ± 133.78 ms for hERG$_T$ and 554.26 ± 75.84 ms for WT hERG ($p < .05$). During the command to 0 mV, the rise-time τ was 577.61 ± 113.09 ms for hERG$_T$ and 296.28 ± 56.92 ms for WT ($p < .05$). At + 20 mV, however, there was no significant difference between hERG$_T$ (188.39 ± 64.30 ms) and WT hERG (78.27 ± 6.77 ms; $p = .07$).

3.3 | Comparison of inactivation characteristics between WT and hERG$_T$ I_{hERG}

We proceeded to determine the voltage dependence of I_{hERG} inactivation (availability) by using the protocol shown in the upper panel of Figure 3a, in the protocol

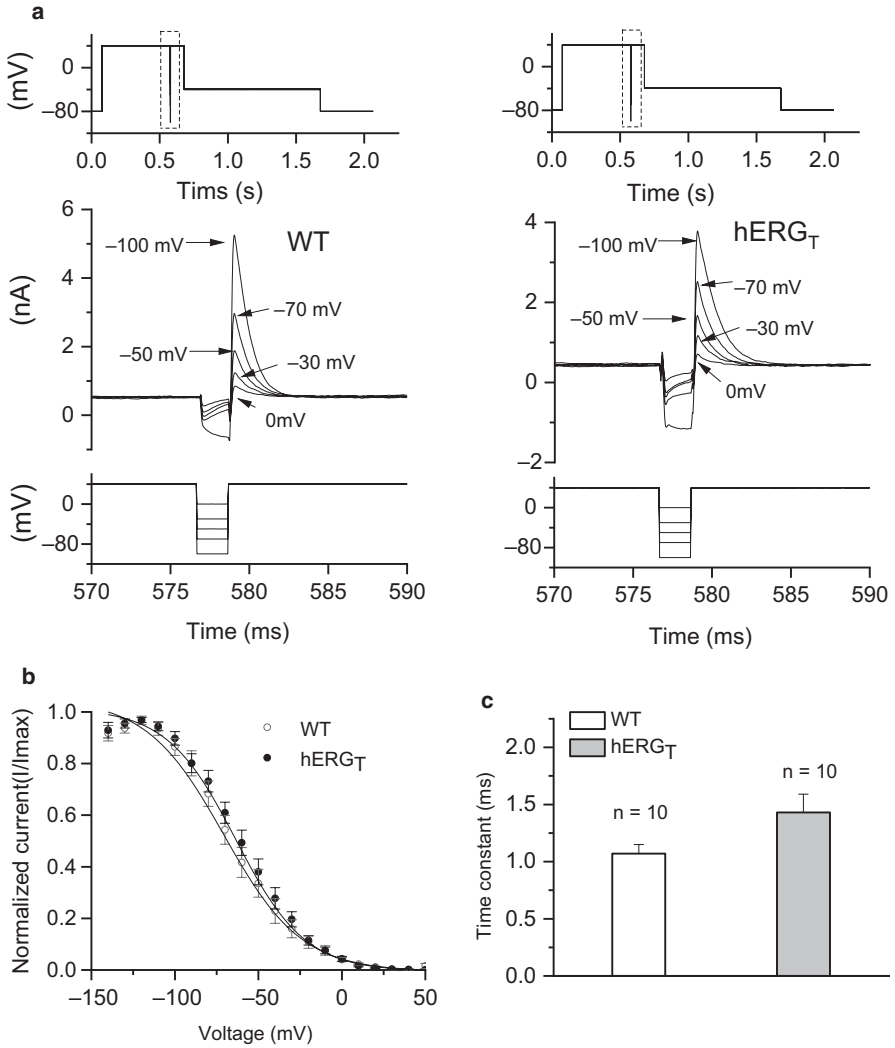

FIGURE 3 Voltage and time-dependence of inactivation for WT and hERG$_T$ I_{hERG}. (a) Upper panels show the whole protocol used to interrogate inactivation, with the highlighted area shown enlarged in the main panels. Main panels show representative traces of WT (Left panel) and hERG$_T$ (right panel) I_{hERG}, focusing on the current profile during the second and start of the third steps of the protocol, only selected traces shown for clarity of display. Relevant portion of voltage protocol shown below currents. (b) I_{hERG} availability plots for WT ($n = 10$) and hERG$_T$ ($n = 10$). Data were fitted with equation 2 to give the $V_{0.5}$ and k values presented in the Results text. (c) Bar chart showing the time constant for development of inactivation of WT ($n = 10$) and hERG$_T$ I_{hERG} ($n = 10$) obtained by single exponential fitting of the currents elicited following the repolarizing step to −120 mV.

(Zhang et al., 2011; Butler *et al*., 2019). An initial depolarizing command to +40 mV was used to activate and then inactivate I_{hERG}; following this, a 2 ms brief repolarizing command was applied to a range of potentials (in 10 mV increments down to −140 mV) to relieve inactivation to varying extents. This was followed by a third step to +40 mV. The magnitude of peak current elicited by the third step reflected the extent of availability induced by the second step (Butler et al., 2019; Zhang et al., 2011). Figure 3a shows representative traces from WT (middle left panel) and hERG$_T$ I_{hERG} (middle right panel) respectively. To correct for possible deactivation during this protocol as in previous work from our laboratory, a method described by Zou *et al* was used (McPate, Duncan, Milnes, Witchel, & Hancox, 2005; Zhang et al., 2011; Zou, Xu, & Sanguinetti, 1998). Peak current amplitudes during the third pulse were obtained by single exponential fitting of the currents and extrapolation to the start of the third step (McPate et al., 2005; Zhang et al., 2011; Zou et al., 1998). Peak currents during the third step were then normalized to maximal current and mean data were plotted as shown in Figure 3b, Boltzmann fitting this relation, using equation 2, yielded an inactivation $V_{0.5}$ value of −66.33 ± 5.38 mV ($k = 18.27 \pm 1.69$; $n = 10$) for WT and −59.99 ± 3.92 mV for hERG$_T$ I_{hERG} ($k = 19.96 \pm 2.26$, $n = 10$, $p > .05$ for $V_{0.5}$ ($p = .35$) and for k ($p = .56$) compared with WT).

The time course of development of inactivation was quantified by mono-exponential fitting of the decline of I_{hERG} transients following repolarization steps to −120 mV in this protocol. The inactivation τ-values obtained from this are shown in Figure 3c; these were 1.07 ± 0.08 ms ($n = 10$) and 1.43 ± 0.16 ms for WT and hERG$_T$ I_{hERG} respectively ($n = 10$). Although there was a trend towards a slowed inactivation time course for hERG$_T$ I_{hERG}, this did not attain statistical significance ($p = .07$, Student t test).

The time course of recovery of I_{hERG} from inactivation was assessed using a protocol (Figure 4) in which a depolarization step to +40 mV was first applied for 500 ms to activate and inactivate I_{hERG}; this was followed by a repolarisation step to −40 mV (a voltage close to which peak I_{hERG} occurs during physiological repolarization (McPate et al., 2009)) for increasing periods of time (between 2 and 20 ms) to release

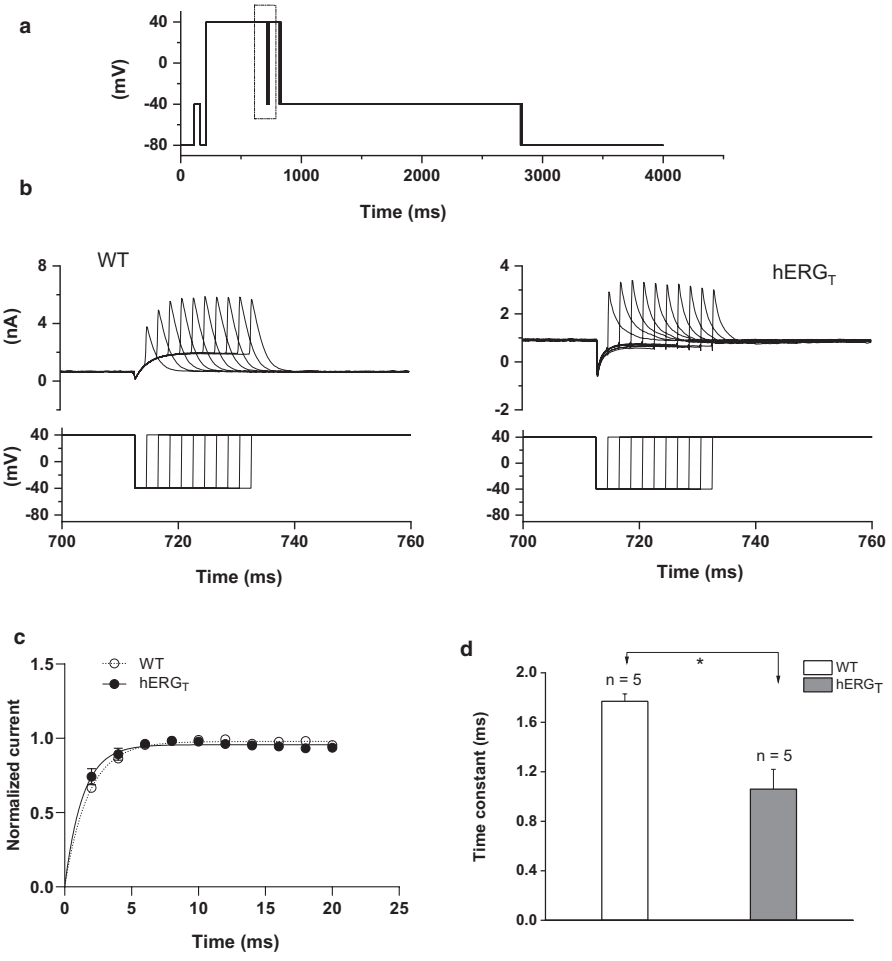

FIGURE 4 Time course of recovery from inactivation for WT and $hERG_T$. (a) Whole protocol used to assess the time course of recovery of I_{hERG} from inactivation, with highlighted area shown in the lower panel of panel 4B. (b) Representative traces of WT and $hERG_T$ I_{hERG} with corresponding portion of the voltage protocol shown below the current traces. (c) Mean normalized current plot with time. The dashed line denotes mono-exponential fit to WT data (open circles, $n = 5$). The solid line denotes mono-exponential fit to $hERG_T$ (filled circles, $n = 5$). (d) Bar chart showing the comparison of recovery time constants for WT ($n = 5$) and $hERG_T$ I_{hERG} ($n = 5$, * denotes statistical significance of $p < .05$; Student's *t* test)

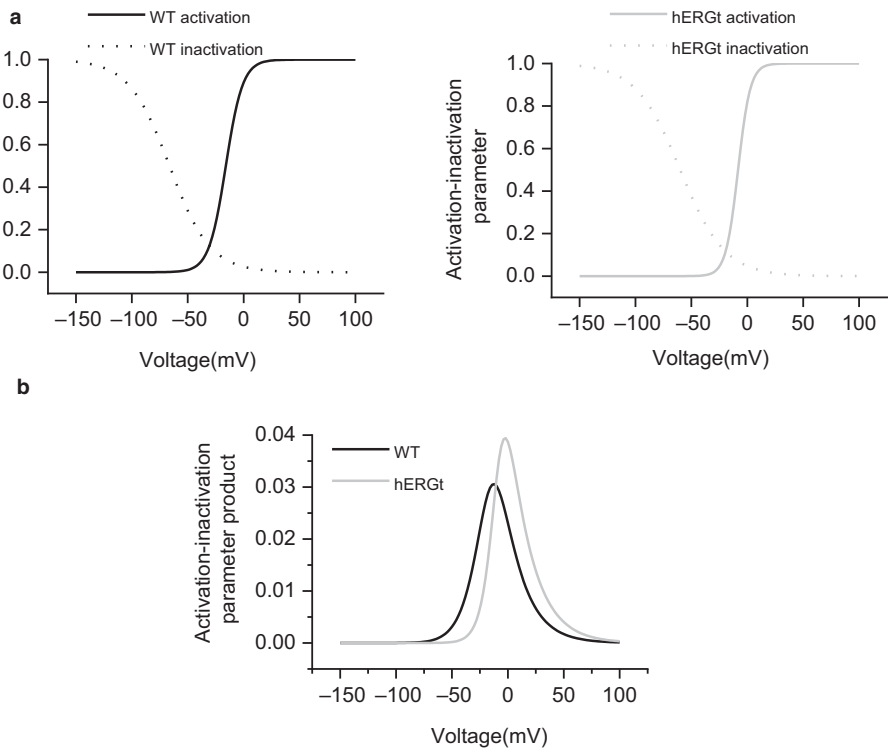

FIGURE 5 WT and $hERG_T$ window current. (a) Superimposed activation (solid line) and inactivation (availability, dashed line) relations for WT (black, left panel) and $hERG_T$ (gray, right panel) I_{hERG} respectively. Activation and inactivation parameters were calculated at 2-mV intervals, using the $V_{0.5}$ and *k* values obtained from fitting the experimental data. (b) "Window current" (the product of activation-inactivation parameters) plotted against membrane potential to show the steady-state WT (in black) and $hERG_T$ (in gray) I_{hERG} window.

inactivation. A second depolarization step to +40 mV was then applied for 100 ms and the I_{hERG} measured, (Figure 4a). From this, the rate of recovery of I_{hERG} from inactivation was quantified by mono-exponentially fitting the transient peak currents following different duration steps to −40 mV (McPate et al., 2009; Zhang et al., 2011). Representative traces for WT and $hERG_T$ I_{hERG} during this protocol are shown in Figure 4b with the lower panel showing the corresponding voltage protocol. The initial two $hERG_T$ records with this protocol (upper right panel of Figure 4b) attained a greater proportion of maximal current amplitude than was the case for WT hERG (upper left panel of Figure 4b), suggestive of faster recovery from inactivation. Peak outward transient currents were normalized to the maximal current observed during the protocol and the resulting mean data were plotted against the duration of the repolarization step. These relations were fitted with a mono-exponential function, giving τ values of 1.77 ± 0.06 ms for WT ($n = 5$) and 1.06 ± 0.16 ms for $hERG_T$ ($n = 5$; $p < .05$, Student's t test). Thus, $hERG_T$ I_{hERG} exhibited significantly accelerated recovery of inactivation.

The $V_{0.5}$ and k values obtained from the activation and inactivation fits to experimental data were used to calculate activation and inactivation parameters for I_{hERG} carried by WT and $hERG_T$ over a wide range of voltages, as plotted in Figure 5a, left and right panel, respectively. The product of activation and inactivation parameters at each membrane potential was calculated and plotted as shown in Figure 5b, in order to obtain "window" current for WT hERG and $hERG_T$ (Butler et al., 2019; Zhang et al., 2011). The I_{hERG} window was slightly rightward shifted and exhibited a modest increase in the peak of the window for $hERG_T$.

3.4 | I_{hERG} profile during ventricular AP clamp compared between WT and $hERG_T$

The AP clamp technique enables membrane potential "history" to be taken into account during dynamic activation of an ionic current of interest (Hancox et al., 1998; Noble, Varghese, Kohl, & Noble, 1998; Zhou et al., 1998). It therefore allows currents to be measured with their normal physiological time course and voltage dependence. Figure 6a shows mean normalized I_{hERG} traces for WT (left panel) and $hERG_T$ (gray trace in right panel with WT current superimposed in black), elicited by the ventricular AP command shown. WT I_{hERG} was initially small, then increased progressively through the AP plateau phase up to a peak before declining during terminal AP repolarisation; the maximal current for WT hERG occurred at −29.84 ± 1.98mV ($n = 10$) (Hancox et al., 1998; McPate et al., 2005, 2009). The mean normalized I_{hERG} for $hERG_T$ appeared to be bigger throughout the AP plateau phase, peaking slightly earlier during the AP. We measured the current integral (area under curve, normalized to cell capacitance) for each channel. Figure 6b compares the total charge carried by WT and $hERG_T$ under AP clamp, the current integral for $hERG_T$ was significantly larger than that for WT hERG ($p < .05$, Student's t test, $n = 10$ for each). While plots of the mean voltage at which maximal current was recorded during repolarization (Figure 6c) showed a modest shift of ~+4 mV (to −25.81 ± 2.51 mV; $n = 10$) for $hERG_T$ compared to the WT channel, this difference did not attain statistical significance ($p = .25$, Student's t test).

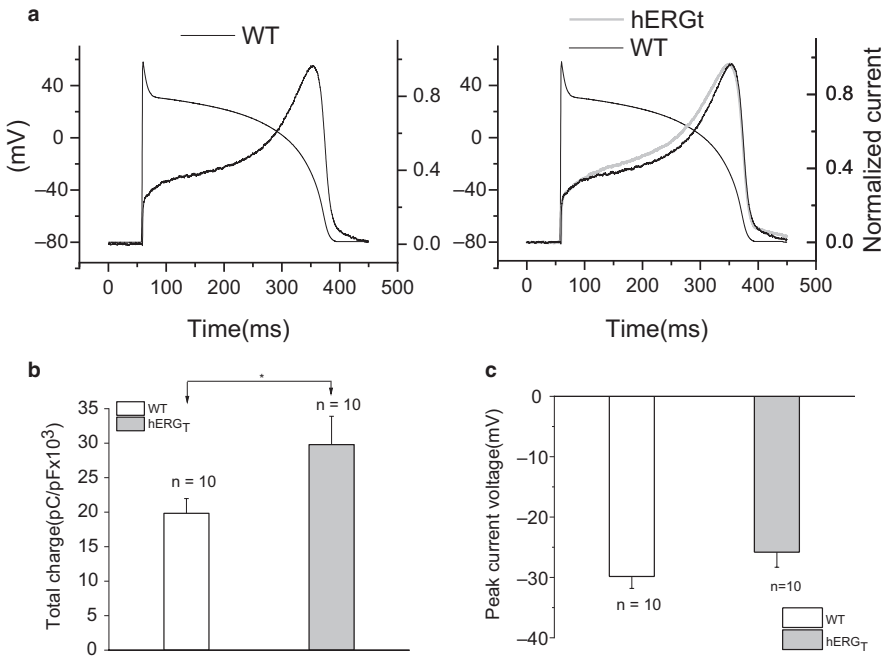

FIGURE 6 I_{hERG} during AP clamp for WT and $hERG_T$. (a) Ventricular AP command waveform overlying mean normalized value of I_{hERG} for WT (left panel in black, $n = 10$) and $hERG_T$ (right panel in gray, $n = 10$, with corresponding WT current superimposed in black). (b) Comparison of the total charge carried by each channel ($n = 10$ for each) during each action potential, calculated by integrating the current traces, normalized to cell capacitance, * denotes statistical significance of $p < .05$; Student's t test. (c) Comparison of the voltage at which the peak currents occurred during AP repolarization for each of WT and $hERG_T$ I_{hERG}

4 | DISCUSSION

To our knowledge, the only prior information on the electrophysiological properties of the $hERG_T$ deletion construct comes from the original cryo-EM study (Wang & MacKinnon, 2017), reporting a +5mV shift in activation $V_{0.5}$ at ambient temperature. Here, we observed a ~+8mV activation $V_{0.5}$ shift at 37°C, together with a rightward shift in window current, slowed deactivation, slightly accelerated recovery from inactivation, and increased current integral during an applied AP command. Several aspects of these findings are worthy of discussion.

4.1 | Relating observed changes in kinetics to channel structure?

Similar to other voltage-gated K^+ channels, functional hERG channels are comprised of a tetramer of subunits containing six transmembrane segments, with a voltage sensor domain (VSD) comprised of S1–S4 segments. In contrast to many other Kv channels, however, the cryo-EM structure of hERG shows a lack of domain-swapping and the VSD is in close apposition to the pore domain of the same subunit (Butler et al., 2020; Robertson & Morais-Cabral, 2019; Wang & MacKinnon, 2017). Voltage-dependent inactivation occurs at the outer mouth of the channel, with comparison of $hERG_T$ and $hERG_{TS}$-S631A (impaired inactivation) mutant structures showing subtle differences in the position of side chains at the outer portion of the selectivity filter (Robertson & Morais-Cabral, 2019; Wang & MacKinnon, 2017).

Deletion of the N terminal hERG-specific domain between residues 138–373 has previously been reported to produce a negative shift in voltage-dependent activation of I_{hERG}, (Viloria, Barros, Giraldez, Gomez-Varela, & de la Pena, 2000), implicating this region in modulation of activation kinetics. Within this stretch of the N terminus lies a "KIKER" sequence (K362-R366). When the positively charged residues in this sequence were substituted by glutamic acid (EIEEE), a markedly negative (~ −41 mV) voltage-shift in activation $V_{0.5}$ was observed (Saenen, Labro, Raes, & Snyders, 2006). On the other hand, when the negatively charged glutamate was substituted by arginine (E365R) a marked positive shift in activation $V_{0.5}$ was observed. E365R also showed slightly slowed deactivation (Saenen et al., 2006). The authors of this study concluded that the modulatory effects of the proximal domain on hERG gating are largely electrostatic and localized to the KIKER region (Saenen et al., 2006). The N terminal deletion region of $hERG_T$ includes residues 141–350 upstream of the KIKER sequence. It is notable that a larger proximal deletion of residues 141–380 ($hERG_{TS}$), which includes the KIKER sequence, resulted in a marked negative shift of $V_{0.5}$ (−20 mV (Wang & MacKinnon, 2017)). It is plausible, therefore, that the 141–350 deletion influences the availability of KIKER residues to undergo electrostatic interactions with the VSD, producing a modest effect on activation kinetics seen here.

Deletion of the hERG N terminus has been found to alter hERG channel inactivation, likely by removing an N terminus interaction with the internal S4–S5 linker region of the channel (Wang, Trudeau, Zappia, & Robertson, 1998). This is believed to account for altered rectification of heteromeric hERG1a/1b channels, which possess fewer hERG1a N termini to interact with the S4–S5 linker than do tetrameric hERG 1a channels (Sale et al., 2008). We found that inactivation kinetics of the $hERG_T$ channel were similar to those of WT hERG, with the only observed difference being a significant acceleration in the recovery of I_{hERG} from inactivation; this may reflect a subtle difference in N terminal interactions with the S4–S5 linker in the $hERG_T$ channel.

Slow deactivation of hERG involves an interaction between the N terminal PAS domain and the C terminal cyclic nucleotide binding domain (CNBD; (Gustina & Trudeau, 2011)). The cryo-EM structures for hERG identified a cytosolic ring structure with the PAS domain of one subunit interacting with the CNBD domain of its neighbor (Wang & MacKinnon, 2017). hERG channels with deletions of CNBD (deletion of residue 749–872) show accelerated deactivation kinetics, whereas deletion of C terminal residues 873–1159 leaves WT activation and deactivation properties unaffected (Gustina & Trudeau, 2011). Muskett *et al* implicated interactions between N terminal residues 1–26 and residues 843, 847 and 850 in the CNBD in I_{hERG} deactivation (Muskett et al., 2011). These residues are proximal to the deleted region from 871 to 1,005 in $hERG_T$, however, so it is not obvious how this deletion could influence deactivation of $hERG_T$ $I_{hERG.}$ On the other hand, residues in the S4–S5 linker provide potential interaction sites for domains that influence stability of the open state and, thereby, deactivation kinetics (Ng et al., 2012). Altered N terminal S4–S5 interactions may therefore account for the slowed I_{hERG} deactivation of $hERG_T$ channels. Some studies reporting substantial C terminal deletions in hERG showed these to be associated with reduced current magnitude (Mihic, Chauhan, Gao, Oudit, & Tsushima, 2011; Nof et al., 2010), which is not the case for $hERG_T$ here. The basis for this difference is not clear, though it is notable that $hERG_T$ involves an excision of part of the C terminus that leaves more than 150 of the final residues intact, while the mutations in these two studies (Mihic et al., 2011; Nof et al., 2010) involved frameshifts and premature stop codons. Thus, they do not mirror the C terminal change made to $hERG_T$.

An additional point of note regarding the $hERG_T$ construct is that we did not observe significantly reduced functional expression (measured as current density) between WT and $hERG_T$ constructs. A number of long QT 2 (LQT2)

missense mutations have been reported within the deleted regions (Anderson et al., 2014; Tester, Will, Haglund, & Ackerman, 2005). In the N terminus, this includes G238S, G306W, S320L, R328C (Tester et al., 2005) and P334L (Lupoglazoff et al., 2001). In the distal C terminus this includes A913V and R1005Q (Anderson et al., 2014); the latter residue is part of the RXR C terminal endoplasmic reticulum (ER) retention signal (Kupershmidt et al., 2002). The C terminal deletion in $hERG_T$ disrupts this ER retention signal. Clearly the overall effects of deletion of the two stretches of N and C termini in $hERG_T$ are not to produce channels with an LQT phenotype.

4.2 | Implications of $hERG_T$ properties for interpretation of pharmacology in light of the hERG cryo-EM structure

A motivator for this study was an apparent deviation between mutagenesis experiments and docking simulations using the hERG cryo-EM structure for a minimally structured, high affinity hERG inhibitor (Helliwell et al., 2018). In the cryo-EM structure, the side chains of F656, which are important for hERG inhibition by multiple drugs (reviewed in Butler et al., 2020), project away from the central pore; a small clockwise rotation of the inner (S6) helix of the hERG pore from its configuration in the cryo-EM structure was suggested to optimize F656 side chain positions for drug interactions consistent with electrophysiological data (Chen, Seebohm, & Sanguinetti, 2002; Helliwell et al., 2018). An independent study has also reported difficulty using docking to the cryo-EM structure in recapitulating experimental data that implicate residue T623 (near the base of the selectivity filter/pore helix) in R-roscovitine binding (Cernuda et al., 2019). Two broad possibilities can account for such differences between in vitro and docking observations: (i) deletions necessary for successful protein purification might affect the channel conformation in ways that are adverse to drug binding and (ii) the channel is essentially normal, but the structure obtained from cryo-EM may have been captured in a nonoptimal configuration for drug binding (Butler et al., 2020; Robertson & Morais-Cabral, 2019). In the cryo-EM structure the S4 voltage sensor was captured in the activated (depolarized), configuration at a nominal potential of 0 mV, and the inner helical gate is open (Wang & MacKinnon, 2017). The information in this study most relevant to this situation is the steady-state window I_{hERG} (Figure 5). 0 mV is close to the peak of the window current for $hERG_T$, while it is a little beyond the peak of the window current for the WT channel. It seems unlikely that this small difference would result in large conformational differences between the pore of WT and $hERG_T$ channels. Thus, it seems more likely that the cryo-EM structure captured a low affinity open state in which the positions of binding residues are nonoptimally configured for interaction with some drugs (Helliwell et al., 2018), although recent studies indicate that the energetic barriers to reorientation of Phe side chains into configurations more optimal for interaction with drugs may be small (Dickson, Velez-Vega, & Duca, 2020; Negami, Araki, Okuno, & Terada, 2019). There are only limited data available on the pharmacology of $hERG_T$ channels (Wang & MacKinnon, 2017) and, with the properties of $hERG_T$ I_{hERG} now more fully characterized, we suggest that future comparison be made of effects on drug binding of mutations to key binding residues in the canonical drug binding between WT and $hERG_T$. If such mutations similarly affect drug binding to the two channels, this will fully eliminate a role for the deletions in $hERG_T$ in influencing drug binding; in that event, the "snapshot" conformation in which the cryo-EM structure was obtained will be the likely explanation for differences between experimental and docking findings (Cernuda et al., 2019; Helliwell et al., 2018).

4.3 | Limitations and conclusions

This study has focused on comparing WT and $hERG_T$ I_{hERG} under basal conditions. The deleted regions in $hERG_T$ contain phosphorylation sites for modulation by protein kinases A and C (PKA and PKC) (Cockerill et al., 2007; Cui, Melman, Palma, Fishman, & McDonald, 2000; Thomas et al., 2003). The well-known K897T polymorphism, which also introduces a phosphorylation site (Gentile et al., 2008) lies within the portion of the C terminus deleted in $hERG_T$. Consequently, while our data indicate that the differences between WT and $hERG_T$ I_{hERG} are modest under basal recording conditions, there could be substantial differences in the response of the two channels to PKA or PKC agonism. In this study, we have not compared pharmacological responses of WT and $hERG_T$ channels, but this is warranted for future studies. We conclude that at physiological temperature, $hERG_T$ channels exhibit rightward voltage-shifted activation, slowed deactivation and faster recovery from inactivation than does WT hERG. Steady-state window current is also rightward shifted for $hERG_T$ channels. These changes are likely to result, at least in part, from altered electrostatic interactions between the intracellular N terminus and other domains of the hERG channel.

ACKNOWLEDGEMENTS

The authors gratefully acknowledge funding from the British Heart Foundation (PG/17/89/33414 to JCH and CED)

CONFLICT OF INTEREST

No conflicting interests, financial or otherwise, are declared by the authors.

AUTHOR CONTRIBUTIONS

Conceptualization and research design: Hancox, Dempsey, and Zhang. Experimentation and data acquisition: Zhang. Data analysis: Zhang. Data interpretation and discussion: Zhang, Hancox, and Dempsey. Wrote or contributed to the writing of the manuscript: Hancox, Zhang, Dempsey.

ETHICAL STATEMENT

This study was conducted on recombinant hERG channel proteins heterologously expressed in HEK 293 cells and involved no work on human or animal primary tissues.

ORCID

Christopher E. Dempsey https://orcid.org/0000-0002-1933-7805
Jules C. Hancox https://orcid.org/0000-0002-2055-6482

REFERENCES

Anderson, C. L., Kuzmicki, C. E., Childs, R. R., Hintz, C. J., Delisle, B. P., & January, C. T. (2014). Large-scale mutational analysis of Kv11.1 reveals molecular insights into type 2 long QT syndrome. *Nature Communications*, *5*, 5535.

Butler, A., Helliwell, M. V., Zhang, Y., Hancox, J. C., & Dempsey, C. E. (2020). An Update on the Structure of hERG. *Front Pharmacol*, *10*, 1572. https://doi.org/10.3389/fphar.2019.01572

Butler, A., Zhang, Y., Stuart, A. G., Dempsey, C. E., & Hancox, J. C. (2018). Action potential clamp characterization of the S631A hERG mutation associated with short QT syndrome. *Physiol Rep*, *6*, e13845. https://doi.org/10.14814/phy2.13845

Butler, A., Zhang, Y., Stuart, A. G., Dempsey, C. E., & Hancox, J. C. (2019). Functional and pharmacological characterization of an S5 domain hERG mutation associated with short QT syndrome. *Heliyon*, *5*, e01429. https://doi.org/10.1016/j.heliyon.2019.e01429

Cernuda, B., Fernandes, C. T., Allam, S. M., Orzillo, M., Suppa, G., Chia, C. Z., … Buraei, Z. (2019). The molecular determinants of R-roscovitine block of hERG channels. *PLoS One*, *14*, e0217733. https://doi.org/10.1371/journal.pone.0217733

Chen, J., Seebohm, G., & Sanguinetti, M. C. (2002). Position of aromatic residues in the S6 domain, not inactivation, dictates cisapride sensitivity of HERG and eag potassium channels. *Proceedings of the National Academy of Sciences of the United States of America*, *99*, 12329–12333. https://doi.org/10.1073/pnas.192367299

Cockerill, S. L., Tobin, A. B., Torrecilla, I., Willars, G. B., Standen, N. B., & Mitcheson, J. S. (2007). Modulation of hERG potassium currents in HEK-293 cells by protein kinase C. Evidence for direct phosphorylation of pore forming subunits. *Journal of Physiology*, *581*, 479–493.

Colenso, C. K., Sessions, R. B., Zhang, Y. H., Hancox, J. C., & Dempsey, C. E. (2013). Interactions between voltage sensor and pore domains in a hERG K^+ channel model from molecular simulations and the effects of a voltage sensor mutation. *Journal of Chemical Information and Modeling*, *53*, 1358–1370.

Cui, J., Melman, Y., Palma, E., Fishman, G. I., & McDonald, T. V. (2000). Cyclic AMP regulates the HERG K+ channel by dual pathways. *Current Biology*, *10*, 671–674. https://doi.org/10.1016/S0960-9822(00)00516-9

Dickson, C. J., Velez-Vega, C., & Duca, J. S. (2020). Revealing Molecular Determinants of hERG Blocker and Activator Binding. *Journal of Chemical Information and Modeling*, *60*, 192–203. https://doi.org/10.1021/acs.jcim.9b00773

Gentile, S., Martin, N., Scappini, E., Williams, J., Erxleben, C., & Armstrong, D. L. (2008). The human ERG1 channel polymorphism, K897T, creates a phosphorylation site that inhibits channel activity. *Proceedings of the National Academy of Sciences of the United States of America*, *105*, 14704–14708. https://doi.org/10.1073/pnas.0802250105

Gintant, G. A. (2008). Preclinical Torsades-de-Pointes screens: Advantages and limitations of surrogate and direct approaches in evaluating proarrhythmic risk. *Pharmacology & Therapeutics*, *119*, 199–209. https://doi.org/10.1016/j.pharmthera.2008.04.010

Gustina, A. S., & Trudeau, M. C. (2011). hERG potassium channel gating is mediated by N- and C-terminal region interactions. *Journal of General Physiology*, *137*, 315–325. https://doi.org/10.1085/jgp.201010582

Hancox, J. C., Levi, A. J., & Witchel, H. J. (1998). Time course and voltage dependence of expressed HERG current compared with native 'rapid' delayed rectifier K current during the cardiac ventricular action potential. *Pflugers Archiv - European Journal of Physiology*, *436*, 843–853. https://doi.org/10.1007/s004240050713

Hancox, J. C., McPate, M. J., El Harchi, A., & Zhang, Y. H. (2008). The hERG potassium channel and hERG screening for drug-induced torsades de pointes. *Pharmacology and Therapeutics*, *119*, 118–132. https://doi.org/10.1016/j.pharmthera.2008.05.009

Hancox, J. C., Whittaker, D. G., Du, C., Stuart, A. G., & Zhang, H. (2018). Emerging therapeutic targets in the short QT syndrome. *Expert Opinion on Therapeutic Targets*, *22*, 439–451. https://doi.org/10.1080/14728222.2018.1470621

Helliwell, M. V., Zhang, Y., El Harchi, A., Du, C., Hancox, J. C., & Dempsey, C. E. (2018). Structural implications of hERG K+ channel block by a high affinity minimally-structured blocker. *Journal of Biological Chemistry*, *293*, 7040–7057.

Jurman, M. E., Boland, L. M., Liu, Y., & Yellen, G. (1994). Visual identification of individual transfected cells for electrophysiology using antibody-coated beads. *BioTechniques*, *17*, 876–888.

Kupershmidt, S., Yang, T., Chanthaphaychith, S., Wang, Z., Towbin, J. A., & Roden, D. M. (2002). Defective human Ether-a-go-go-related gene trafficking linked to an endoplasmic reticulum retention signal in the C terminus. *Journal of Biological Chemistry*, *277*, 27442–27448.

Lu, Y., MahautSmith, M. P., Varghese, A., Huang, C. L. H., Kemp, P. R., & Vandenberg, J. I. (2001). Effects of premature stimulation on HERG channels. *Journal of Physiology*, *537*(3), 843–851.

Lupoglazoff, J. M., Denjoy, I., Berthet, M., Neyroud, N., Demay, L., Richard, P., … Guicheney, P. (2001). Notched T waves on Holter recordings enhance detection of patients with LQT2 (HERG) mutations. *Circulation*, *103*, 1095–1101.

McPate, M. J., Duncan, R. S., Milnes, J. T., Witchel, H. J., & Hancox, J. C. (2005). The N588K-HERG K^+ channel mutation in the 'short QT syndrome': Mechanism of gain-in-function determined at 37°C. *Biochemical and Biophysical Research Communications*, *334*, 441–449. https://doi.org/10.1016/j.bbrc.2005.06.112

McPate, M. J., Zhang, H., Adeniran, I., Cordeiro, J. M., Witchel, H. J., & Hancox, J. C. (2009). Comparative effects of the short QT N588K mutation at 37°C on hERG K^+ channel current during ventricular, Purkinje fibre and atrial action potentials: An action potential clamp study. *Journal of Physiology and Pharmacology*, *60*, 23–41.

Melgari, D., Brack, K. E., Zhang, C., Zhang, Y., El Harchi, A., Mitcheson, J. S., … Hancox, J. C. (2015). hERG potassium channel blockade by the HCN channel inhibitor bradycardic agent ivabradine. *Journal of the American Heart Association*, *4*, e001813. https://doi.org/10.1161/JAHA.115.001813

Mihic, A., Chauhan, V. S., Gao, X., Oudit, G. Y., & Tsushima, R. G. (2011). Trafficking defect and proteasomal degradation contribute to the phenotype of a novel KCNH2 long QT syndrome mutation. *PLoS One*, *6*, e18273. https://doi.org/10.1371/journal.pone.0018273

Mitcheson, J. S., & Hancox, J. C. (1999). An investigation of the role played by the E-4031-sensitive (rapid delayed rectifier) potassium current in isolated rabbit atrioventricular nodal and ventricular myocytes. *Pflugers Archiv - European Journal of Physiology*, *438*, 843–850. https://doi.org/10.1007/s004240051114

Muskett, F. W., Thouta, S., Thomson, S. J., Bowen, A., Stansfeld, P. J., & Mitcheson, J. S. (2011). Mechanistic insight into human ether-a-go-go-related gene (hERG) K^+ channel deactivation gating from the solution structure of the EAG domain. *Journal of Biological Chemistry*, *286*, 6184–6191.

Negami, T., Araki, M., Okuno, Y., & Terada, T. (2019). Calculation of absolute binding free energies between the hERG channel and structurally diverse drugs. *Scientific Reports*, *9*, 16586. https://doi.org/10.1038/s41598-019-53120-6

Ng, C. A., Perry, M. D., Tan, P. S., Hill, A. P., Kuchel, P. W., & Vandenberg, J. I. (2012). The S4–S5 linker acts as a signal integrator for HERG K^+ channel activation and deactivation gating. *PLoS One*, *7*, e31640.

Noble, D., Varghese, A., Kohl, P., & Noble, P. (1998). Improved guinea-pig ventricular cell model incorporating a diadic space, I_{Kr} and I_{Ks}, and length- and tension-dependent processes. *Canadian Journal of Cardiology*, *14*, 123–134.

Nof, E., Cordeiro, J. M., Perez, G. J., Scornik, F. S., Calloe, K., Love, B., … Antzelevitch, C. (2010). A common single nucleotide polymorphism can exacerbate long-QT type 2 syndrome leading to sudden infant death. *Circulation: Cardiovascular Genetics*, *3*, 199–206. https://doi.org/10.1161/CIRCGENETICS.109.898569

Ono, K., & Ito, H. (1995). Role of rapidly activating delayed rectifier K current in sinoatrial node pacemaker activity. *American Journal of Physiology*, *269*, H453–H462. https://doi.org/10.1152/ajpheart.1995.269.2.H453

Robertson, G. A., & Morais-Cabral, J. H. (2019). hERG function in light of structure. *Biophysical Journal.118*(4), 790–797.

Rocchetti, M., Besana, A., Gurrola, G. B., Possani, L. D., & Zaza, A. (2001). Rate dependency of delayed rectifier currents during the guinea-pig ventricular action potential. *Journal of Physiology*, *534*(3), 721–732. https://doi.org/10.1111/j.1469-7793.2001.00721.x

Saenen, J. B., Labro, A. J., Raes, A., & Snyders, D. J. (2006). Modulation of HERG gating by a charge cluster in the N-terminal proximal domain. *Biophysical Journal*, *91*, 4381–4391. https://doi.org/10.1529/biophysj.106.087247

Sale, H., Wang, J., O'Hara, T. J., Tester, D. J., Phartiyal, P., He, J. Q., … Robertson, G. A. (2008). Physiological properties of hERG 1a/1b heteromeric currents and a hERG 1b-specific mutation associated with Long-QT syndrome. *Circulation Research*, *103*, e81–e95. https://doi.org/10.1161/CIRCRESAHA.108.185249

Sanguinetti, M. C., Jiang, C., Curran, M. E., & Keating, M. T. (1995). A mechanistic link between an inherited and an acquired cardiac arrhythmia: HERG encodes the I_{Kr} potassium channel. *Cell*, *81*, 299.

Sanguinetti, M. C., & Tristani-Firouzi, M. (2006). hERG potassium channels and cardiac arrhythmia. *Nature*, *440*, 463–469. https://doi.org/10.1038/nature04710

Shimoni, Y., Clark, R. B., & Giles, W. R. (1992). Role of an inwardly rectifying potassium current in rabbit ventricular action potential. *Journal of Physiology*, *448*, 709–727. https://doi.org/10.1113/jphysiol.1992.sp019066

Su, Z., Brown, E. C., Wang, W., & MacKinnon, R. (2016). Novel cell-free high-throughput screening method for pharmacological tools targeting K^+ channels. *Proceedings of the National Academy of Sciences of the United States of America*, *113*, 5748–5753.

Tamargo, J., Caballero, R., Gomez, R., Valenzuela, C., & Delpon, E. (2004). Pharmacology of cardiac potassium channels. *Cardiovascular Research*, *62*, 9–33. https://doi.org/10.1016/j.cardiores.2003.12.026

ten Tusscher, K. H., Noble, D., Noble, P. J., & Panfilov, A. V. (2004). A model for human ventricular tissue. *Am J Physiology*, *286*, H1573–H1589. https://doi.org/10.1152/ajpheart.00794.2003

Tester, D. J., Will, M. L., Haglund, C. M., & Ackerman, M. J. (2005). Compendium of cardiac channel mutations in 541 consecutive unrelated patients referred for long QT syndrome genetic testing. *Heart Rhythm: the Official Journal of the Heart Rhythm Society*, *2*, 507–517. https://doi.org/10.1016/j.hrthm.2005.01.020

Thomas, D., Zhang, W., Wu, K., Wimmer, A. B., Gut, B., Wendt-Nordahl, G., … Karle, C. A. (2003). Regulation of HERG potassium channel activation by protein kinase C independent of direct phosphorylation of the channel protein. *Cardiovascular Research*, *59*, 14–26. https://doi.org/10.1016/S0008-6363(03)00386-9

Trudeau, M. C., Warmke, J. W., Ganetzky, B., & Robertson, G. A. (1995). HERG, an inward rectifier in the voltage-gated potassium channel family. *Science*, *269*, 92–95.

Vandenberg, J. I., Walker, B. D., & Campbell, T. J. (2001). HERG K^+ channels: Friend and foe. *TIPS*, *22*, 240–246. https://doi.org/10.1016/S0165-6147(00)01662-X

Viloria, C. G., Barros, F., Giraldez, T., Gomez-Varela, D., & de la Peña, P. (2000). Differential effects of amino-terminal distal and proximal domains in the regulation of human erg K^+ channel gating. *Biophysical Journal*, *79*, 231–246. https://doi.org/10.1016/S0006-3495(00)76286-2

Wang, J., Trudeau, M. C., Zappia, A. M., & Robertson, G. A. (1998). Regulation of deactivation by an amino terminal domain in HERG potassium channels. *Journal of General Physiology*, *112*, 637–647.

Wang, W., & MacKinnon, R. (2017). Cryo-EM Structure of the Open Human Ether-a-go-go-Related K^+ Channel hERG. *Cell*, *169*, 422–430.

Zaza, A., Rochetti, M., Brioschi, A., Cantadori, A., & Ferroni, A. (1998). Dynamic Ca^{2+}-induced inward rectification of K^+ current during the ventricular action potential. *Circulation Research*, *82*, 947–956.

Zhang, Y., Colenso, C. K., El Harchi, A., Cheng, H., Witchel, H. J., Dempsey, C. E., & Hancox, J. C. (2016). Interactions between amiodarone and the hERG potassium channel pore determined with mutagenesis and in silico docking. *Biochemical Pharmacology*, *113*, 24–35. https://doi.org/10.1016/j.bcp.2016.05.013

Zhang, Y. H., Colenso, C. K., Sessions, R. B., Dempsey, C. E., & Hancox, J. C. (2011). The hERG K^+ channel S4 domain L532P mutation: Characterization at 37°C. *Biochimica Et Biophysica Acta*, *1808*, 2477–2487. https://doi.org/10.1016/j.bbamem.2011.07.001

Zhou, Z., Gong, Q., Ye, B., Fan, Z., Makielski, J. C., Robertson, G. A., & January, C. T. (1998). Properties of HERG channels stably expressed in HEK 293 cells studied at physiological temperature. *Biophysical Journal*, *74*, 230–241. https://doi.org/10.1016/S0006-3495(98)77782-3

Zou, A., Xu, Q. P., & Sanguinetti, M. C. (1998). A mutation in the pore region of HERG K channels expressed in *Xenopus* oocytes reduces rectification by shifting the voltage dependence of inactivation. *Journal of Physiology*, *509*, 129–137.

How to cite this article: Zhang Y, Dempsey CE, Hancox JC. Electrophysiological characterization of the modified $hERG_T$ potassium channel used to obtain the first cryo-EM hERG structure. *Physiol Rep*. 2020;00:e14568. https://doi.org/10.14814/phy2.14568